JOURNAL OF APPLIED CRYSTALLOGRAPHY

ISSN 1600-5767

Received 15 July 2026
Accepted 3 September 2026

Edited by R. Guinebretière, Institut de Recherche sur les Céramiques, France

Keywords: X-ray back-diffraction; grazing-incidence X-ray diffraction; angular dispersion rate; high-resolution X-ray optical devices.

Experimental observation of grazing-incidence X-ray back-diffraction with large angular dispersion

Shih-Lun Chen,[a,b,c]* Yun-Liang Soo,[b] Bi-Hsuan Lin,[a] Tzu-Hung Chuang,[a] Shih-Chang Weng,[a] Yi-Wei Tsai[a] and Mau-Tsu Tang[a]*

[a]National Synchrotron Radiation Research Center, Hsinchu, 300092, Taiwan, [b]Department of Physics, National Tsing Hua University, Hsinchu, 300044, Taiwan, and [c]International College of Semiconductor Technology, National Yang Ming Chiao Tung University, Hsinchu, 300093, Taiwan. *Correspondence e-mail: cslaaron@nycu.edu.tw, mautsu@nsrrc.org.tw

We report the first experimental observation of grazing-incidence X-ray back-diffraction (GIXBD) exhibiting exceptionally large angular dispersion. An angular dispersion rate (ADR) of 44.4 ± 9.3 μrad meV^{-1} was measured from a Si (12 4 0) crystal with a surface miscut angle of 89.926°, representing the largest ADR reported for X-ray back-diffraction. The observed diffraction behaviour is quantitatively reproduced by the full dynamical theory of X-ray diffraction. A kinematic formulation based on Snell's law provides a simple geometrical interpretation of the grazing-incidence limit beyond the conventional DuMond analysis and predicts a large but finite ADR, thereby avoiding the apparent divergence of the conventional treatment. These results provide the first experimental validation of GIXBD, establish a physically consistent description of angular dispersion in the extreme grazing-incidence limit and provide a sound physical basis for future ultra-high-resolution crystal X-ray optics.

1. Introduction

In X-ray optics, the refractive index of a non-absorbing medium is slightly less than unity, differing from unity by only approximately 10^{-5}–10^{-6} (Als-Nielsen & McMorrow, 2011). Despite this small deviation, it has been exploited in the development of numerous X-ray optical components, including reflective mirrors (Attwood & Sakdinawat, 2017) and compound refractive lenses (Schroer & Lengeler, 2005).

When X-rays are diffracted by a perfect crystal, the effective refractive index differs from the nominal value n_0 owing to the formation of Bloch wavefields arising from multiple elastic scattering within the crystal. In the dynamical theory of X-ray diffraction, the refractive index is represented by the eigenvalues of the wavefields inside the crystal. This theory forms the foundation of modern crystal-based X-ray optics (Shvyd'ko, 2004).

The DuMond diagram, derived from the dynamical theory of X-ray diffraction, provides a graphical representation of the transformation of incident X-rays into diffracted beams in wavelength–angular (or energy–momentum) space (Shvyd'ko, 2004). This approach has been widely applied to multiple-crystal optical systems and has enabled monochromators with energy resolutions approaching $\Delta E/E = 10^{-8}$ (Ishikawa *et al.*, 2005).

Using DuMond analysis, Shvyd'ko *et al.* (2006) showed that the angular dispersion of X-ray back-diffraction (Bragg angle $\theta_B = 90°$) depends strongly on the miscut angle θ_m, which is defined as the angle between the crystal surface and the diffracting atomic planes:

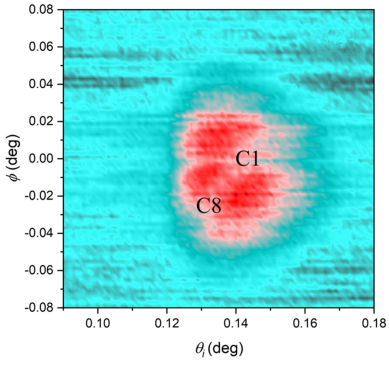

OPEN ACCESS
Published under a CC BY 4.0 licence

$$\delta\theta_f = 2\frac{\delta\lambda}{2d_{hkl}}\tan\theta_m. \quad (1)$$

where $\delta\theta_f$ is the deviation angle. The corresponding angular dispersion rate (ADR = $\delta\theta_f/\delta E$) can be defined as

$$\frac{\delta\theta_f}{\delta E} = \frac{2}{E_0}\tan\theta_m, \quad (2)$$

where E_0 is the exact back-diffraction energy. According to equation (2), the ADR increases rapidly as the miscut angle θ_m approaches 90°, where the angle of incident X-rays approaches the critical angle for total external reflection.

This prediction has stimulated the development of several high-angular-dispersion X-ray optical devices (Stoupin *et al.*, 2013; Shvyd'ko *et al.*, 2014). However, equation (2) predicts an infinite ADR as θ_m approaches 90°, implying an unphysical singularity. Experimentally, the largest ADR reported to date is 8.5 μrad meV^{-1}, obtained from Si (008) back-diffraction (Shvyd'ko *et al.*, 2006), which is comparable to typical angular dispersion values encountered in visible-light optics.

The divergence predicted by equation (2) indicates that the conventional DuMond treatment becomes inadequate in the extreme grazing-incidence limit.

Using the Cartesian-coordinate formalism developed by Stetsko & Chang (1997), our earlier work predicted the intensity distribution and the large but finite ADR of two-beam grazing-incidence X-ray back-diffraction (GIXBD), particularly for miscut angles approaching 90° (Chen *et al.*, 2023).

In this work, we present the first experimental observation of GIXBD from a highly miscut Si (12 4 0) crystal with θ_m = 89.926°. The measured diffraction intensity distributions are quantitatively reproduced by full 24-beam dynamical diffraction calculations. The experimentally determined ADR of 44.4 ± 9.3 μrad meV^{-1} is consistent with both the dynamical theory and the kinematic interpretation developed here, providing the first experimental validation of GIXBD under grazing-incidence conditions. This work therefore bridges the gap between the theoretical prediction of GIXBD and its experimental realization.

2. Physical origin of the ADR

The large angular dispersion predicted for GIXBD originates naturally from the dynamical theory of X-ray diffraction, which fully accounts for multiple scattering inside the crystal. However, despite the complexity of the dynamical treatment, the resulting dispersion can be understood from a remarkably simple geometrical viewpoint. As shown below, the essential behaviour follows directly from Snell's law.

Applying Snell's law at the crystal surface requires continuity of the tangential wavevector component across the interface. This immediately gives (Chen *et al.*, 2023)

$$\cos\theta_{i0}\cos\phi = \cos\theta_c\sin\theta_m. \quad (3)$$

Equation (3) shows that the grazing-incidence angle θ_{i0} is determined jointly by the crystal surface orientation and the critical angle θ_c for total external reflection. The incident geometry is therefore constrained by the nominal refractive index n_0 by

$$n_0 \cong 1 - \frac{1}{2}\theta_c^2 \quad (4)$$

before diffraction takes place.

For the present geometry, θ_c = 0.1219° and the measured miscut angle θ_m = 89.926°. With azimuthal angle ϕ = 0°, substitution into equation (3) yields an incident angle of θ_{i0} = 0.1426°. The same geometrical argument can be extended to explain the origin of angular dispersion. When the photon energy changes while the incident direction is fixed, the tangential wavevector component must remain conserved. Consequently, the back-diffracted beam rotates to satisfy this momentum constraint,

$$k_0(\cos\theta_{f0} + \cos\theta_{i0}) = 2n_0k_0\sin\theta_m. \quad (5)$$

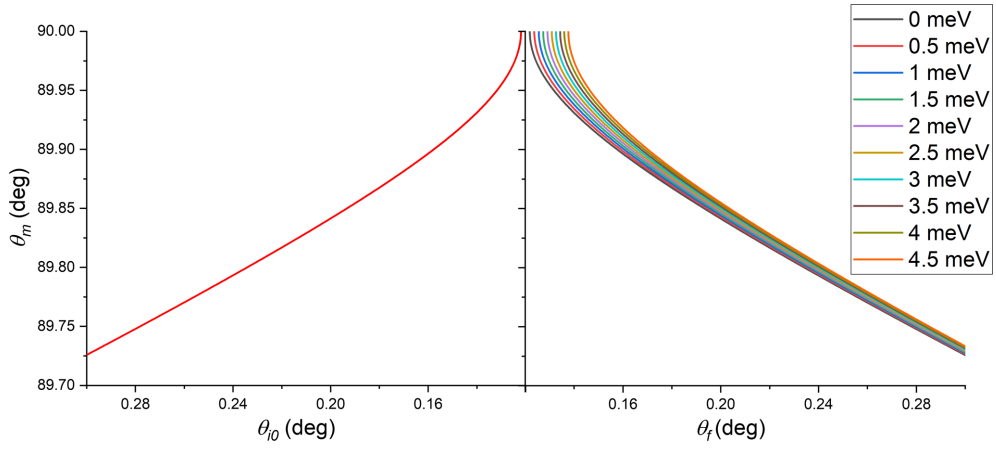

Figure 1
Calculated back-diffracted angle, θ_f, as a function of surface miscut angle, θ_m, for photon-energy offsets $E - E_0$ ranging from 0 to 4.5 meV. The corresponding incident angle θ_{i0} at exact back-diffraction is also shown. The increasing separation of the curves as θ_m approaches 90° illustrates the enhancement of the angular dispersion.

Here k_0 denotes the wavevector magnitude in air, while θ_{i0} and θ_{f0} are the incident and back-diffracted angles at exact back-diffraction, respectively. When the incident photon energy changes while the incident angle remains fixed, conservation of the tangential wavevector component still applies, leading to

$$k(\cos\theta_f + \cos\theta_{i0}) = 2n_0k_0\sin\theta_m, \tag{6}$$

where k denotes the wavevector magnitude at the varying energy.

Using equation (3) together with the relation $k_0/k = E_0/E$, equation (6) can be rewritten as

$$\cos\theta_f = \left(2\frac{E_0}{E} - 1\right)\cos\theta_{i0}. \tag{7}$$

Fig. 1 illustrates the calculated dependence of θ_f on θ_m for photon-energy offsets ranging from 0 to 4.5 meV. As θ_m approaches 90°, the separation between the curves increases rapidly, demonstrating the dramatic enhancement of the angular dispersion predicted by the dynamical theory.

Differentiating equation (7) with respect to the photon energy yields the ADR,

$$\frac{\delta\theta_f}{\delta E} = 2\frac{1}{E_0\tan\theta_{i0}}. \tag{8}$$

Equation (8) shows that the angular dispersion is governed by the grazing-incidence angle rather than the surface miscut angle itself.

The conventional DuMond analysis [equation (2)] predicts that the ADR diverges as the surface miscut angle approaches 90°, leading to an unphysical mathematical singularity. In contrast, the present kinematic formulation naturally removes this divergence because the grazing-incidence angle remains finite through the constraint imposed by Snell's law. Consequently, equations (3) and (8) predict a large but finite ADR that is physically meaningful. The following experimental measurements provide direct verification of this interpretation.

The present kinematic formulation is not intended to replace the rigorous dynamical theory, which remains the quantitative foundation for describing GIXBD. Rather, it provides a simple analytical framework that captures the essential dependence of the angular dispersion on the grazing-incidence geometry. More importantly, the design of high-angular-dispersion crystal optics typically requires exploration of a large parameter space involving crystal reflections, asymmetry angles, grazing-incidence geometries and photon energies. While rigorous multi-beam dynamical calculations remain indispensable for quantitative evaluation, the analytical expression provided by equation (8) enables rapid identification of promising configurations before detailed numerical simulations are undertaken. In this respect, the present formulation plays a role analogous to that of the DuMond diagram in the design of conventional crystal-optical systems.

3. Experimental setup

The experiments were performed at the TPS 09A beamline of the National Synchrotron Radiation Research Center (NSRRC), Taiwan. The experimental arrangement is illustrated in Fig. 2(*a*). The incident X-ray beam was generated by an in-vacuum undulator (IU22) with a 22 mm magnetic period and was initially monochromated by a Si (111) double-crystal monochromator (DCM), providing an energy resolution of $\Delta E/E = 1.4 \times 10^{-4}$.

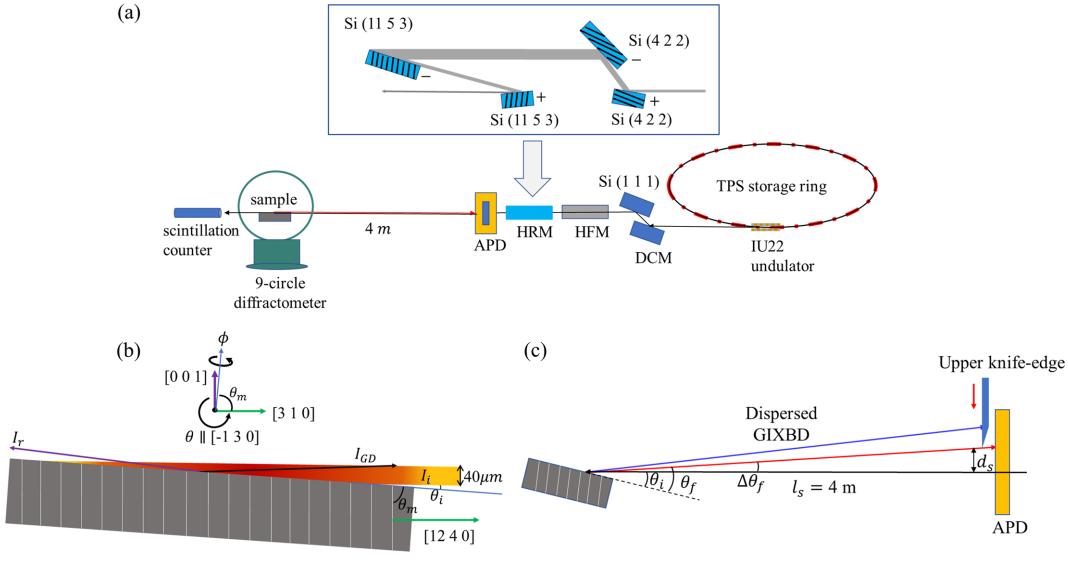

Figure 2
(*a*) Experimental layout at the TPS 09A beamline. An overall energy resolution of 2.8×10^{-8} was achieved using a four-crystal high-resolution monochromator comprising two pairs of highly asymmetrically cut Si crystals. (*b*) Definition of the crystal geometry showing the surface orientation, the diffracting planes, the incident beam and the surface miscut angle used for grazing-incidence X-ray back-diffraction. (*c*) Experimental arrangement used to determine the angular dispersion rate. A knife edge was scanned through the back-diffracted beam to determine its angular position.

The beam was further monochromated using a high-resolution monochromator (HRM) comprising two pairs of highly asymmetrically cut crystals, Si (422) and Si (11 5 3), arranged in a (+ − − +) geometry (Chang *et al.*, 2021). The dispersive pair, consisting of the second Si (422) crystal and the first Si (11 5 3) crystal, provided an overall energy resolution of 2.8×10^{-8}, corresponding to an energy bandwidth of approximately 0.4 meV at 14.4388 keV. This energy bandwidth is substantially narrower than the intrinsic energy width of the Si (12 4 0) back-diffraction reflection (Chang *et al.*, 2005), thereby enabling accurate measurements of the angular dispersion.

The sample was mounted at the centre of a nine-circle diffractometer, allowing independent control of the incident angle (θ_i) and the azimuthal angle (ϕ). A half-transmitting avalanche photodiode (APD) and a scintillation detector were positioned upstream and downstream of the sample, respectively, enabling simultaneous measurements of the incident, back-diffracted and transmitted beams. The APD was located 4 m upstream of the sample. A translation step of 5 µm corresponded to an angular step of approximately 1.25 µrad. A vacuum flight tube was installed between the APD and the sample to minimize X-ray attenuation in air.

This experimental arrangement enables both two-dimensional mapping of the GIXBD intensity distribution and precise measurements of the ADR as described in the following sections.

4. Grazing-incidence X-ray back-diffraction

A highly miscut Si (12 4 0) crystal was used to investigate GIXBD experimentally. The sample was a 20 × 20 mm silicon wafer with its surface normal oriented approximately along the [001] direction. As illustrated in Fig. 2(*b*), the surface miscut angle, θ_m, is defined as the angle between the surface normal and the [12 4 0] crystallographic direction. Throughout the experiment, the incident beam was σ-polarized, with the electric field perpendicular to the diffraction plane.

The vertical beam size at the sample position was measured to be 40 µm using a knife-edge scan. Under the grazing-incidence geometry, this corresponded to a beam footprint of approximately 16 mm full width at half-maximum (FWHM) along the crystal surface, comparable to the 20 mm sample length. The incident photon energy was calibrated by comparing the measured diffraction profiles with dynamical diffraction calculations.

The GIXBD diffraction maps were measured as functions of the incident angle (θ_i) and the azimuthal angle (ϕ). Representative results are shown in Figs. 3(*a*) and 3(*b*) for

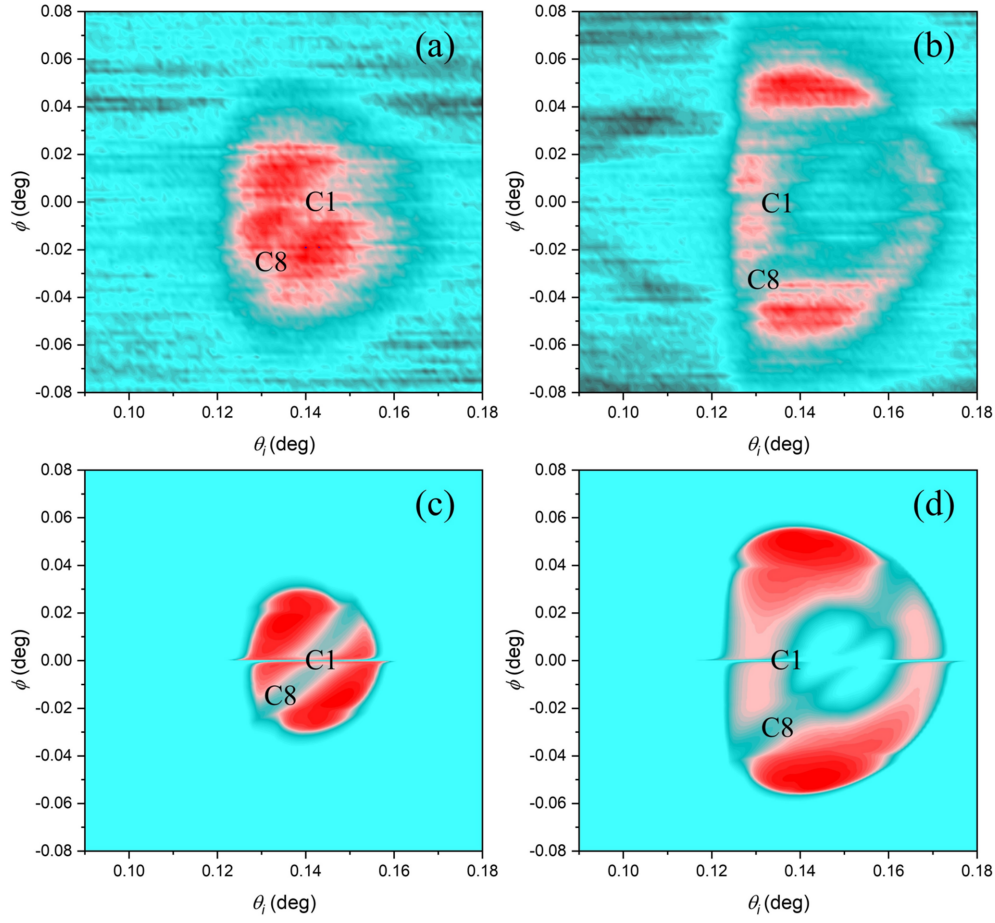

Figure 3
Experimental and simulated GIXBD diffraction maps. (*a*, *b*) Experimental GIXBD measurements for photon-energy offsets of $\Delta E = 0$ and 4.9 meV, respectively. (*c*, *d*) Corresponding 24-beam dynamical diffraction simulations.

photon-energy offsets of $\Delta E = 0$ and 4.9 meV, respectively, relative to the exact back-diffraction energy of 14.4388 keV. The measurements reveal well defined diffraction features whose positions vary systematically with the incident photon energy, consistent with the expected angular-dispersion behaviour.

The calculations to reproduce the measured diffraction patterns contain no adjustable parameters other than the experimentally determined crystal orientation and incident photon energy. The corresponding dynamical diffraction simulations are shown in Figs. 3(*c*) and 3(*d*). Si (12 4 0) back-diffraction intrinsically involves 24-beam diffraction owing to the high crystallographic symmetry of Si. In addition to the (000) incident beam and the (12 4 0) back-diffracted beam, the other 22 multiple-diffraction reflections can be classified into nine coplanar diffraction groups, denoted C1–C9: C1, (12 0 0), (040), (880), (4$\bar{4}$0), (480) and (8$\bar{4}$0); C2, (682) and (6$\bar{4}\bar{2}$); C3, (12 2 $\bar{2}$) and (022); C4, (646) and (60$\bar{6}$); C5, (82$\bar{6}$) and (426); C6, (826) and (42$\bar{6}$); C7, (64$\bar{6}$) and (606); C8, (12 2 2) and (02$\bar{2}$); and C9, (68$\bar{2}$) and (6$\bar{4}$2) (Chang *et al.*, 2005). The calculations were performed using the Cartesian-coordinate formalism developed by Stetsko & Chang (1997), in which all 24 simultaneously excited diffraction channels and the corresponding 96 Bloch-wave eigenmodes were included. Matching the electromagnetic boundary conditions at the crystal surface yielded the external diffracted wavefields and their corresponding intensities.

The calculations reveal several characteristic features that distinguish GIXBD from conventional normal-incidence X-ray back-diffraction (NIXBD). In NIXBD, the large number of simultaneously excited multiple reflections substantially reduces the back-diffraction intensity (Chang *et al.*, 2005; Chiu *et al.*, 2008). Under grazing-incidence conditions, however, the diffraction process becomes strongly constrained by the crystal surface. Consequently, only the C1 and C8 diffraction groups contribute significantly to the intensity redistribution, while the remaining multiple-diffraction channels are largely suppressed.

The C1 group consists of the six reflections (12 0 0), (880), (040), (4$\bar{4}$0), (8$\bar{4}$0) and (480). In reciprocal space, these reflections are coplanar with the incident beam and the primary Si (12 4 0) back-diffraction vector. Their coplanar geometry enables simultaneous excitation with the primary reflection and leads to a pronounced reduction in the GIXBD intensity.

In addition, conservation of energy introduces a correction factor in the dynamical calculations (Shvyd'ko, 2004; Chen *et al.*, 2023). This factor strongly suppresses the C2, C4, C5, C6, C7 and C9 diffraction groups, while leaving the C3 and C8 groups comparatively unaffected. The out-of-phase interference between the two C3 reflections further reduces their contribution, whereas the C8 reflections interfere constructively and therefore remain observable.

Although the detailed treatment of the multiple-diffraction interactions will be presented elsewhere, the present comparison demonstrates that the experimentally observed GIXBD diffraction maps are quantitatively reproduced by the full 24-beam dynamical calculations. This agreement is particularly significant because the simulations were performed using only independently determined experimental parameters, without introducing empirical fitting parameters. The close correspondence between experiment and theory therefore provides the first direct experimental validation of the full dynamical description of GIXBD.

5. ADR measurements

Having established that the GIXBD intensity distributions are accurately described by the full dynamical theory, we next measured the ADR, which constitutes the principal experimental result of this work.

The ADR was determined by fixing the incident angle at θ_{i0} while varying the incident photon energy, ΔE, as expressed by equation (8). The back-diffracted beam was recorded using an APD positioned 4 m upstream of the sample [Fig. 2(*c*)]. To minimize the influence of the intense C1 multiple-diffraction group, the azimuthal angle was offset by -0.003°.

The experimentally measured diffraction intensity was normalized to the incident intensity and corrected for known losses associated with the measurement geometry. These corrections include the APD transmission (∼60%), attenuation along the uncovered air path (∼80% transmission) and the finite interception of the Gaussian beam footprint by the 20 mm-long crystal (∼85%). The corrected intensity is presented as the experimental reflectivity in Fig. 4(*a*).

Representative diffraction profiles measured as functions of the incident angle are shown in Fig. 4(*a*) for photon-energy offsets of 1.0 and 4.4 meV. The corresponding dynamical simulations reproduce both the peak positions and the profile shapes.

The angular position of the back-diffracted beam was determined using a precision knife-edge scan [Fig. 4(*b*)]. The knife edge, with a surface roughness below 1 µm, was translated vertically across the beam immediately downstream of the APD. The beam position was obtained from the derivative of the measured intensity profile, with the peak in the derivative defining the beam centre, as indicated by the dashed lines in Fig. 4(*b*).

To improve statistical precision, measurements obtained at three adjacent incident angles $\theta_{i0} = 0.141^\circ$, 0.142° and 0.143° were combined. Fig. 4(*c*) demonstrates that the experimentally measured beam deviations follow the predictions of the full dynamical calculations. In contrast, the conventional DuMond analysis increasingly deviates from the experimental results as the grazing-incidence geometry approaches the extreme miscut condition. A linear fit to the experimental data yields an angular dispersion rate of 44.4 ± 9.3 µrad meV^{-1}, approximately five times larger than the highest value previously reported (Shvyd'ko *et al.*, 2006).

The dependence of the ADR on the surface miscut angle is summarized in Fig. 5. Predictions obtained from the conventional DuMond analysis, the kinematic prediction and the full dynamical calculations are compared with the experimental measurement. Whereas the DuMond formulation predicts an

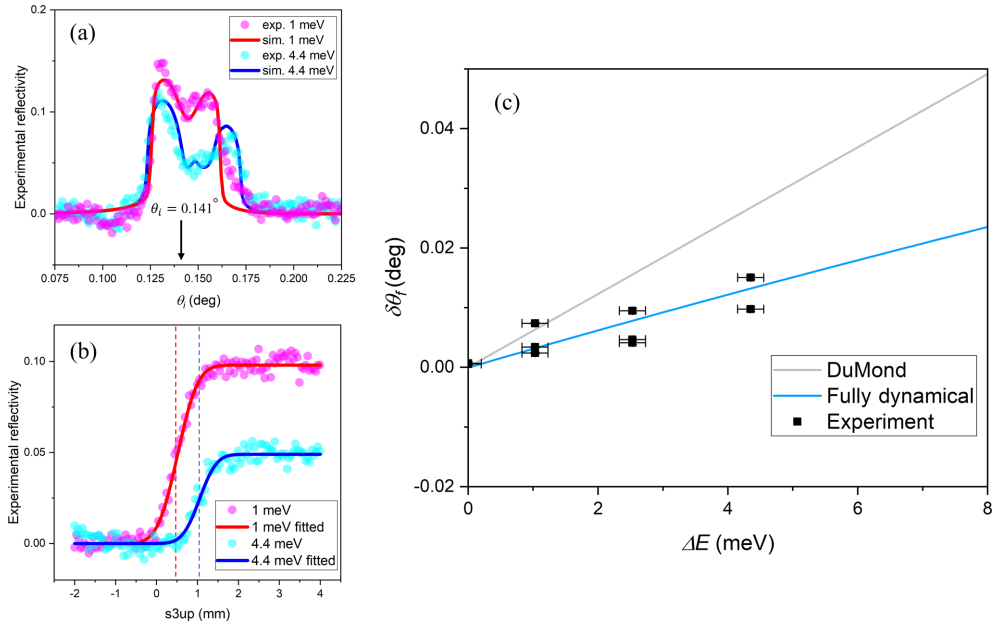

Figure 4
Determination of the ADR. (*a*) Experimental (symbols) and simulated (solid lines) back-diffraction profiles for photon-energy offsets of 1.0 and 4.4 meV. (*b*) Knife-edge scans used to determine the angular position of the back-diffracted beam. The beam centre was obtained from the derivative of the intensity profile. (*c*) Measured beam deviation as a function of photon-energy offset compared with predictions from the conventional DuMond analysis and the full dynamical calculations.

unphysical divergence as θ_m approaches 90°, both the kinematic and dynamical treatments yield finite ADR values. The experimentally measured ADR falls within the range predicted by these two independent approaches, providing strong experimental support for the revised physical interpretation developed in Section 2.

Because the kinematic prediction is derived solely from geometrical considerations based on Snell's law, its close agreement with experiment demonstrates that the large angular dispersion observed in GIXBD has a simple geometrical origin while remaining fully consistent with the rigorous dynamical theory.

The calculated reflectivity of the Si (12 4 0) back-diffraction reflection is also included in Fig. 5. Although the ADR increases rapidly as the surface miscut angle approaches 90°, the reflectivity decreases in the same region. This behaviour illustrates the practical trade-off between maximizing angular dispersion and maintaining diffraction efficiency when selecting the crystal geometry for high-resolution X-ray optics.

The experimentally determined reflectivity at $\theta_{i0} = 0.141^\circ$, after correction for the known intensity losses described above, is approximately 0.10. This value remains lower than the intrinsic reflectivity of approximately 0.44 predicted by the 24-beam plane-wave dynamical calculation. A substantial contribution to this remaining difference may arise from the finite experimental angular resolution. The calculated intrinsic angular width is approximately 0.0012°, whereas the experimentally observed width is approximately 0.003°. As a first-order estimate, assuming conservation of the integrated diffracted intensity, the corresponding broadening reduces the peak reflectivity by a factor of approximately 0.0012/0.003 $\simeq$ 0.4. Applying this factor to the calculated intrinsic reflectivity gives an expected broadened peak reflectivity of approximately 0.18. Although still higher than the experimental value of approximately 0.10, the difference is substantially reduced. The residual discrepancy may arise partly from the crystal surface quality, which can be particularly important under the extreme grazing-incidence conditions employed here, as well as from the approximate treatment of the instrumental broadening. Importantly, these effects influence the peak

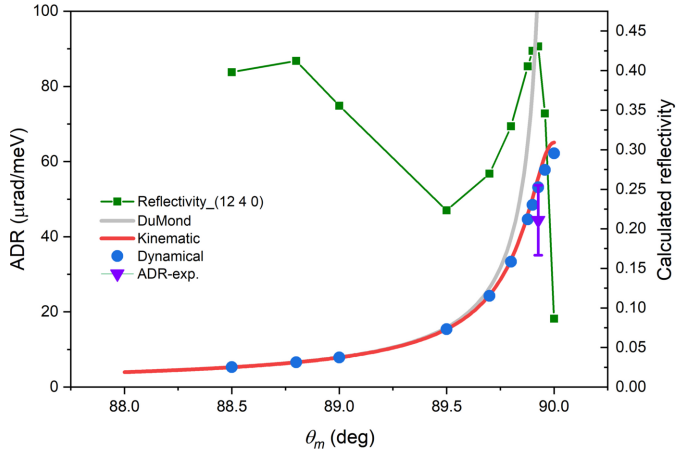

Figure 5
Comparison of ADRs predicted by the conventional DuMond analysis, the kinematic prediction and the full dynamical calculations as functions of the surface miscut angle. The experimental ADR measured in the present work is also shown. Unlike the DuMond analysis, both the kinematic and dynamical treatments predict finite ADR values as the miscut angle approaches 90°. The calculated intrinsic reflectivity of the Si (12 4 0) back-diffraction reflection is shown on the right-hand axis. It corresponds to an ideal Si crystal under the plane-wave approximation and does not include experimental resolution effects.

intensity but do not significantly affect the angular positions used to determine the ADR.

6. Conclusion

In summary, we have presented the first experimental observation of GIXBD from a highly miscut Si (12 4 0) crystal. The measured diffraction intensity distributions are quantitatively reproduced by full 24-beam dynamical diffraction calculations, providing the first direct experimental validation of the theoretical description of GIXBD.

The measured ADR is accurately reproduced by the rigorous dynamical calculations and is naturally explained by a simple kinematic formulation based on Snell's law. Unlike the conventional DuMond treatment, which predicts an apparent divergence as the surface miscut angle approaches 90°, the present formulation predicts a large but finite ADR that is confirmed experimentally. Beyond providing physical insight into the origin of the observed dispersion, the analytical expression offers a practical framework for rapidly exploring and optimizing grazing-incidence high-angular-dispersion crystal optics before undertaking detailed multi-beam dynamical calculations.

Taken together, these results establish a physically consistent description of angular dispersion in GIXBD and provide a foundation for future developments in ultra-high-resolution crystal X-ray optics. Because the energy resolution of angular-dispersive optical systems scales directly with the ADR (Stoupin *et al.*, 2013; Shvyd'ko *et al.*, 2014), the exceptionally large ADR demonstrated here suggests that GIXBD offers a promising route towards future sub-100 µeV crystal monochromators and analyzers. The detailed optical implementation of such systems is beyond the scope of the present work and will be reported separately.

Acknowledgements

We are indebted to the NSRRC staff for their technical assistance.

Conflict of interest

The authors declare no conflicts of interest.

Data availability

Data underlying the results presented in this paper are not publicly available at this time but may be obtained from the authors upon reasonable request.

Funding information

SLC thanks the National Science and Technology Council of Taiwan and the National Synchrotron Radiation Research Center for financial support.

References

Als-Nielsen, J. & McMorrow, D. (2011). *Elements of Modern X-ray Physics*. John Wiley & Sons.
Attwood, D. & Sakdinawat, A. (2017). *X-rays and Extreme Ultraviolet Radiation: Principles and Applications*, 2nd ed. Cambridge University Press.
Chang, S. L., Stetsko, Y. P., Tang, M. T., Lee, Y. R., Sun, W. H., Yabashi, M. & Ishikawa, T. (2005). *Phys. Rev. Lett.* **94**, 174801.
Chang, Y. Y., Tsai, Y. W., Weng, S. C., Chen, S. L. & Chang, S. L. (2021). *Opt. Lett.* **46**, 416–419.
Chen, S. L., Soo, Y. L., Lin, B. H., Chuang, T. H. & Tang, M. T. (2023). *Opt. Express* **31**, 41864–41874.
Chiu, M.-S., Stetsko, Yu. P. & Chang, S.-L. (2008). *Acta Cryst.* A**64**, 394–403.
Ishikawa, T., Tamasaku, K. & Yabashi, M. (2005). *Nucl. Instrum. Methods Phys. Res. A* **547**, 42–49.
Schroer, C. G. & Lengeler, B. (2005). *Phys. Rev. Lett.* **94**, 054802.
Shvyd'Ko, Y. (2004). *X-ray Optics: High-Energy-Resolution Applications*. Springer Science & Business Media.
Shvyd'ko, Y., Stoupin, S., Shu, D., Collins, S. P., Mundboth, K., Sutter, J. & Tolkiehn, M. (2014). *Nat. Commun.* **5**, 4219.
Shvyd'ko, Y. V., Lerche, M., Kuetgens, U., Rüter, H. D., Alatas, A. & Zhao, J. (2006). *Phys. Rev. Lett.* **97**, 235502.
Stetsko, Yu. P. & Chang, S.-L. (1997). *Acta Cryst.* A**53**, 28–34.
Stoupin, S., Shvyd'ko, Y. V., Shu, D., Blank, V. D., Terentyev, S. A., Polyakov, S. N., Kuznetsov, M. S., Lemesh, I., Mundboth, K., Collins, S. P., Sutter, J. P. & Tolkiehn, M. (2013). *Opt. Express* **21**, 30932–30946.